Supporting Online Material for

The Impact of Boreal Forest Fire on Climate Warming

J. T. Randerson,* H. Liu, M. G. Flanner, S. D. Chambers, Y. Jin, P. G. Hess, G. Pfister, M. C. Mack, K. K. Treseder, L. R. Welp, F. S. Chapin, J. W. Harden, M. L. Goulden, E. Lyons, J. C. Neff, E. A. G. Schuur, C. S. Zender

*To whom correspondence should be addressed. E-mail: jranders@uci.edu

Published 17 November 2006, *Science* **314**, 1130 (2006)
DOI: 10.1126/science.1132075

This PDF file includes:

Supporting Online Material

Materials and Methods
SOM Text
Figs. S1-S10
Tables S1 and S2
References and notes

1. Supporting materials and methods

Overview

Here we present details of the approaches we used to quantify the different forcing agents associated with the Donnelly Flats fire, which burned during 11-18 June 1999 in interior Alaska (63°, 55′ N; 145°, 44′ W) as a result of human ignition. As described in the main text, we developed radiative forcing estimates for the first year immediately after fire and over a period of 80 years after fire (including the first year). The longer interval represented the amount of time required for the vegetation to recover to a pre-fire state that was defined by our control stand. This fire was so small that it had a minor effect on the global radiation budget. Nevertheless, working out the contribution of the various forcing agents and their combined effect for a single fire is a necessary step towards assessing the impact of a changing boreal fire regime on climate at regional or continental scales.

Radiative forcing: Definition and Units

In the main text and supporting online material, we consider the influence of 1 m^2 of burned area from the Donnelly Flats fire. We consider the fire emissions from this 1 m^2 in terms of their influence on global annual mean radiative forcing from long-lived greenhouse gases, tropospheric O_3, the direct effect of atmospheric aerosols, and deposition of black carbon on remote snow and ice. We also estimate radiative forcing from post-fire changes in surface albedo within the burn perimeter. We follow the Intergovernmental Panel on Climate Change (IPCC) Third Assessment Report (TAR) definition of radiative forcing. Specifically, radiative forcing is defined as the change in net radiation at the tropopause caused by the forcing agent, after the stratosphere adjusts radiatively to the agent (*1*).

We report global annual mean radiative forcing (in W) per m^2 of burned area. By 'global' we mean, for example, that we considered the perturbation to the Earth's total radiation budget from CO_2 pulse released by the fire mixing uniformly throughout the atmosphere. Similarly, for the aerosol and ozone forcings, the mixing pattern was non-uniform, and so we summed the perturbation from the fire to the radiation budget across the Earth's entire surface (across all of the atmospheric model grid cells). As described above, the radiative forcing estimates in Table 1 and throughout the main text include stratospheric adjustment, and so to compare directly with Intergovernmental Panel on Climate Change Third Assessment Report estimates (*1*) they should be divided by the area of the earth. More detailed information about our approach for estimating radiative

forcing is provided in section 1.11. In several cases we had to convert from instantaneous forcing at the tropopause to adjusted forcing (the IPCC standard) using published estimates of how these two quantities are related (*2, 3*).

1.1 Estimating carbon emissions from the Donnelly Flats fire

We used a combination of standard inventory and allometric methods (*4*) with a survey of burn severity to estimate biomass and carbon of trees greater than 1.37 m in height consumed in the 1999 Donnelly Flats fire. Within the eddy covariance tower footprint, 16 plots (100 m^2 each) were established in four blocks (n = 4) with greater than 100 m between blocks. The diameter at breast height (DBH; 1.37 m) was measured and burn severity was estimated for all trees (standing and fallen) in these plots. Burn severity was assigned a percent score for each of the following classes: needles consumed, fine branches consumed, coarse branches consumed, cones consumed, and bark consumed. Site-specific allometric equations based on DBH (M.C. Mack, unpublished data) were then used to calculate pre-fire biomass pools for each tree. Biomass pools were assumed to consist of 50% carbon. Carbon lost per tree was calculated as the sum of pre-fire pools multiplied by the fraction of the pool consumed during the fire. Trees were summed within plots, and divided by 100 m^2 to yield C loss per m^2. Biomass loss from the vascular plant understory was calculated as the difference between the mean of post-fire aboveground understory biomass (immediately following the fire) in ten 1 m^2 plots randomly distributed in the tower footprint of the burn site and the mean understory biomass in the control site tower footprint.

Total carbon loss from surface soils, non-vascular plants, and lichens during the Donnelly Flats fire was estimated in two ways by Neff et al. (*5*). The first involved directly measuring the change in total soil organic matter (SOM) between 8 control plots and 6 burn plots. A second approach involved using Al (a non-volatile element conserved during the fire) to estimate the fuel loads and loss within individual burned plots, via a comparison with the Al to C ratio of SOM in the control plots. Carbon transferred from aboveground vegetation to the soil during and immediately after fire is accounted for in these soil measurements. These two approaches yielded slightly different estimates: 1071 ± 537 g C m^{-2} and 1421 ± 267 g C m^{-2}, respectively. Here we used the average of these two approaches 1246 ± 600 g C m^{-2}.

1.2 Estimating additional carbon losses during the first year after fire

We estimated additional soil respiration carbon losses during year 1 using a combination of chamber, eddy covariance, and modeling approaches. Chamber measurements of soil respiration were made at six sites within the eddy covariance tower footprint four times a day, for a total of eight days between the 5th and 26th of July 1999. A LI-COR 6200 portable photosynthesis system was used in conjunction with a 20 cm diameter (8 L Plexiglas) chamber within which the air was circulated using a pair of slow moving 50 mm fans (*6*). The chamber was allowed to equilibrate to ambient pressure via a 20 cm length of 1 mm inner diameter copper tubing mounted through the top of the chamber. Each measurement consisted of ten CO_2 concentration observations at eight-second intervals. A regression of CO_2 with time was then performed from which respiration estimates were made based on chamber temperature, humidity, and ambient pressure. For each measurement the chamber was clamped to pre-installed PVC collars that were each left in position for the duration of the measurement period. The collars

were each cut at least 10 cm into the charred surface using a sharpened soil corer so that they were firmly seated in mineral soil. The mean and standard error of the chamber observations during July was 1.5 ± 0.2 μmol m^{-2} s^{-1}.

We used a combination of 3-D ultrasonic anemometer (Solent 1199HSH, Gill Instruments Ltd., England) and closed-path, infrared-absorption H_2O/CO_2 gas analyzer (IRGA: LI-6262, LI-COR Inc., Lincoln, NB, U.S.A.) to make flux measurements within the Donnelly Flats burn scar during July 1999 and during March – June of 2000. We mounted the sonic anemometer and IRGA intake on a 3 m boom, at a height of 5.1 m, on a 15 m aluminum tower (Climatronics Corp., Bohemia, NY, U.S.A.). Since the longest and most homogeneous fetch regions of the burn scar extended north, east and south of the measurement site, and prevailing winds were usually oriented north-south, we oriented the mounting boom approximately east/northeast.

The IRGA was aspirated at approximately 8 liters min^{-1} using a diaphragm pump (UN815-KTDC, KNF Neuberger, Trenton, NJ, U.S.A.) via a 3.3 mm internal diameter "Bev-a-Line" intake tube (Thermoplastic Processes Inc., Sterling, NJ, U.S.A.). This flow rate was sufficient to rapidly flush the IRGA's optical bench as well as maintain turbulent flow in the sampling line, important requirements for performing eddy-covariance flux measurements with a closed-path analyzer. We installed a 1.3 liter PVC buffer volume between the diaphragm pump and the IRGA to reduce pressure pulsing effects. We constructed the initial 1.5 m of the IRGA's intake line from insulated copper tubing to minimize temperature-induced density fluctuations in the sample air stream (*7*).

We performed two-point (zero and span) calibrations on the IRGA for water vapor and CO_2 at regular intervals. The zero calibration was performed using ultra-high purity nitrogen. Span checks for water vapor and CO_2 were performed using a precision dew-point generator (LI-610, LI-COR Inc.) and a balanced CO_2 standard, respectively. Prior to calculating the turbulent fluxes we performed a coordinate rotation of the wind vector such that the u component was inline with the sonic axis (*8*). To account for slight variations in sample flow rate due to varying pump performance and ambient wind conditions, we calculated, and corrected for, the lag time between the sonic anemometer and IRGA signals for each 30-minute block of data. Under conditions when the lag time was poorly defined (typically near neutral stability), we adopted the daily modal lag time. We linearly detrended each 30-minute data block to remove contributions from scales of turbulence too large to be sampled within that time period. We made the final flux estimates by taking 30-minute averages over the diurnal cycle.

With closed path IRGAs in particular, there are several factors that contribute independently to underestimated flux estimates, including: the distance between instruments, instrument response time and signal attenuation (*9*). We adopted an approach that involved the calculation of an "induction factor" to account for the discrepancy between the observed and an idealized cospectrum as a result of the collective system inadequacies (*10*). The induction factor is unique to a given instrumental setup and, once determined, can be applied to the whole measurement period. The factor with which we eventually corrected the covariance estimates was determined separately for each 30-minute block as a function of the induction factor, measurement height, wind speed and atmospheric stability (equations 32 and 33 in (*10*) for unstable and stable conditions, respectively). All post processing was performed using a FORTRAN time series analysis package called 'RAMF' version 8.1 (*11*). Eddy flux measurements during July of 1999 during the same times as the chamber measurements yielded a net flux of 1.8 ± 0.3 μmol m^{-2} s^{-1}. We averaged the eddy covariance and

chamber estimates of CO_2 flux from July to obtain a flux estimate of 1.7 ± 0.3 μmol m^{-2} s^{-1}.

From eddy covariance measurements made during the following spring, we obtained flux estimates of 0.46 ± 0.41, 0.49 ± 0.49, and 0.49 ± 0.53 μmol m^{-2} s^{-1} for April, May, and the first part of June. For the period in between these two measurement periods (August-March), we constructed a simple temperature-dependent model with a Q_{10} of 2 based on monthly mean surface air temperatures. We adjusted the baseline soil respiration rate such that the model and measured fluxes optimally matched both the July and the following May flux data. For the modeled fluxes we assumed an error of ± 50% reflecting uncertainties in our understanding of the temperature sensitivity of respiration and winter controls on microbial processes. The sum of modeled losses over this interval was 99 ± 49 g C m^{-2}. The total ecosystem respiratory loss during the first post-fire year was 202 ± 53 g C m^{-2} yr^{-1}.

1.3 Post-fire net ecosystem production (NEP) trajectory

To construct a trajectory of post-fire carbon accumulation (fig. S3A), we used three constraints. The first was that after 80 years (the approximate age of the adjacent control stand) the ecosystem accumulated as much carbon as was lost during the first year of the fire (fig. S3B). This constraint ensured consistency with the observations from the control site that were used to estimate the pre-fire duff layer thickness and the allometry relationships used to estimate the loss of aboveground biomass.

Second, we assumed that the annual rate of carbon accumulation was greatest during a deciduous phase from 10 to 40 years. The basis for this constraint was a series of eddy covariance CO_2 flux measurements that we made during 2002-2004 within the perimeter of the Donnelly Flats fire, in a stand that burned in 1987, and in the control. The eddy covariance system used during this latter period consisted of a CSAT3 sonic anemometer (Campbell Sci Ltd., Logan, UT, USA) and LiCor 7500 CO_2/H_2O IRGA (LICOR Inc., Lincoln, NB, USA). Details of the eddy covariance calculations are provided in Liu et al. (*12*) and Welp et al. (*13*). Integrated carbon uptake during the growing season (May-September), was -31 ± 20 g C m^{-2} at the Donnelly Flats fire, -191 ± 33 g C m^{-2} at the Granite Creek fire that burned in 1987, and -152 ± 9 g C m^{-2} at the control stand averaged over 2002-2004 (and with standard deviations reflecting interannual variability in fluxes). Growing season net CO_2 uptake was greatest in the deciduous forest (fig S4) and provides partial evidence for high rates of C accumulation during intermediate stages of succession. These eddy covariance measurements from the fire chronosequence also provide some evidence that the transition from a net source in the first year after fire to a net sink occurs within the first decade. This result is consistent with the moderate to severe burn severity observed within the perimeter of the Donnelly Flats fire (*5*); much of the soil organic C pool was consumed during the fire, leaving a relatively small pool available for decomposition.

A third constraint was that after 40 years (the end of the deciduous phase), the rate of C accumulation slowed following an exponential function and with a relaxation time of 75 years. This ensured that after 150 years, the carbon balance of the forest was close to steady state, and consistent with observations from other older black spruce stands (*14*). A slowing of the carbon accumulation rate of this magnitude is also consistent with first-order decomposition and accumulation rate constants derived from radiocarbon

measurements in other boreal forest stands with feathermoss ground cover (*15*). Trumbore and Harden (*15*) predicted accumulation rates of approximately 12 ± 13 g C m^2 yr^{-1} and 4 ± 2 g C m^2 yr^{-1} for feathermoss and sphagnum cover, respectively for an approximately 150 year old black spruce (OBS) site in Canada. With the NEP curve shown in fig. S3A, we estimate NEP to be 7 g C m^2 yr^{-1} at 150 years after fire. We recognize that our accumulation rates are lower than other reported trajectories in the boreal forest (*16, 17*) and attribute this to the well-drained soils and lack of permafrost at our sites that probably slowed rates of both vegetation and soil carbon accumulation. We assumed that other carbon gain/loss pathways, including leaching and organic C losses were negligible so that NEP was equal to net ecosystem carbon balance (NECB) (*18*).

1.4 Estimating the radiative forcing from fire emissions of CO_2 and CH_4

We used the total carbon emissions estimates described in section 1.1 along with emissions factors (*19*) and the assumption that 0.50 g C corresponds to 1 g biomass to estimate fluxes of CO_2 and CH_4 from the fire. We assumed that these trace gases were instantly well mixed in the global atmosphere, that all CO was oxidized to CO_2, and that for the first year, all of the CO_2 and CH_4 emitted by the fire remained airborne. We also considered the indirect production of CH_4 via temporary suppression of atmospheric OH levels by fire-emitted CO (*20-22*). We assumed that 100 molecules of fire-emitted CO was equivalent to 8 additional molecules of CH_4 (*21*). Radiative forcing from CO_2 and CH_4 was estimated using equations (and updated constants) from Table 3 of Myhre et al. (*23*). Radiative forcing from CO_2 and CH_4 during year 1 was 8.0 ± 3.3 W m^{-2}, with 6.0 ± 2.1 W m^{-2} from CO_2, 1.0 ± 0.4 W m^{-2} from direct CH_4 emissions, and 1.0 ± 0.6 W m^{-2} from indirect effects of CO on the background CH_4 reservoir. Our error estimate includes a component from emissions (± 2.8 W m^{-2}) and a component associated with our subjective assessment of the uncertainty associated with the radiative transfer model (± 0.5 W m^{-2}).

After the first year, we allowed the fire-emitted CH_4 (and its influence on radiative forcing) to decrease with an atmospheric lifetime of 10 years, reflecting oxidation by OH and other sink processes. Fire-emitted CO_2 was removed from the atmosphere by two sinks: the accumulation of carbon in the recovering post-fire ecosystem and via ocean exchange. In considering this single fire, we assumed the rest of the terrestrial biosphere was neither a sink nor a source. Our approach for estimating the post-fire trajectory of net ecosystem production (NEP) and subsequent carbon accumulation is described in section 1.3. Ocean uptake of the fire-emitted CO_2 pulse was estimated using an impulse response function from the Joos and Siegenthaler ocean carbon model as described by Enting et al. (2001). This response function (fig. S3C) was constructed assuming that the emitted pulse occurred at contemporary CO_2 levels and that fossil fuel emissions continue on a trajectory required for stabilization of atmospheric CO_2 at 650 ppm by 2100 (*24*). In each year after fire, ocean exchange acted only upon the component of the fire-emitted CO_2 pulse that remained in the atmosphere (that wasn't taken up in previous time steps by regrowing vegetation or by ocean exchange).

The atmospheric CO_2 anomaly resulting from the combined effect of the ocean and post-fire carbon sinks is shown in fig. S3D. Radiative forcing from CO_2 and CH_4 during years 0-80 (and reflecting this atmospheric CO_2 trajectory) was 1.6 ± 0.8 W m^{-2}.

For this longer interval, our error estimate includes the components described above for year 1 as well as an additional 20% reflecting uncertainty introduced from estimating the post-fire atmospheric greenhouse gas trajectory.

1.5 Radiative forcing derived from observed changes in surface albedo

The instantaneous radiative forcing at the tropopause from a change in surface albedo due to fire is approximately equal to the difference in outgoing shortwave radiation between the control and burn sites, after this difference has been attenuated by clouds and other atmospheric constituents within the troposphere. Equivalently, it is the difference in net radiation at the tropopause caused by changes in surface albedo. We used the column radiation model (CRM; (*25, 26*)) to estimate net changes in tropopause radiation fluxes, starting with our measurements of surface albedo.

We constructed monthly mean estimates of incoming shortwave radiation (S_{in}) and outgoing shortwave radiation (S_{out}) from the Eppley precision spectral radiometers mounted on our towers (figs. S5 and S6). We constructed monthly mean values during 2002-2004, corresponding to a mean of years 3-5 after fire. Instrument heights and other details about our micrometeorological measurements are described by Liu et al. (*12*). The ratio of the monthly mean values of S_{out} and S_{in} were used to construct monthly mean values of surface albedo (fig. S7).

With CRM, we made four sets of model runs: with and without cloud cover and with control and burn surface albedo. For all simulations we used monthly mean profiles of atmospheric temperature, specific humidity, and ozone from the European Centre for Medium-Range Weather Forecasts 40 years Reanalysis product (*27*) and we assumed an aerosol optical depth of 0.14. For the cloud cover simulations, we imposed a single 100% cloud cover layer in the model at the 974 mb level, with a liquid water content of 100 g m^{-2}. For each set of model runs, we made a simulation for each hour of each month (a total of 288 simulations) to capture both diurnal and seasonal variations in solar geometry. We assumed the tropopause corresponded to the 198 mb level in the model.

Estimates of S_{in} at our sites from the clear sky and cloudy sky model simulations bracket our tower observations (fig. S5). We then solved for the clear sky and cloudy sky fractions each month that matched our monthly observations of S_{in}. These fractions were then used to combine the clear sky and cloudy sky model estimates of tropopause net radiation from the control and burn albedo simulations. Finally, we took the difference between tropopause net radiation between the control and burn albedo simulations (weighted by the appropriate clear sky and cloudy sky fractions) as our estimate of instantaneous radiative forcing at the tropopause (fig. S8). Based on a series of published climate simulations (*2, 3*) we assumed that stratospheric adjustment to changes in surface albedo was negligible and so the instantaneous forcing at the tropopause was equal to the IPCC definition of adjusted radiative forcing. In this analysis, we found that the difference in annual outgoing shortwave radiation at the tropopause was 60% of the difference in outgoing shortwave radiation at the surface.

Clouds, aerosols, and trace gases accounted for a 40% annual reduction of the outgoing surface signal using the CRM. The difference in S_{out} (control – burn) at the surface was -13.9 ± 3.0 W m^{-2} (fig. S8). The difference at the tropopause, which is approximately equal to the radiative forcing from the surface albedo changes, was -8.4 W

m^{-2}. This value represents the mean from 2002-2004. Our error estimate for this forcing reflects both interannual variability in S_{out} caused by variations in snow cover (± 1.8 W m^{-2}) and a subjective assessment of uncertainty introduced from the use of the CRM (± 1.0 W m^{-2}) for a total of ± 2.8 W m^{-2}. For this period, 3-5 years after fire, summer albedo was higher in the recent burn than in the control from the establishment of grasses, small shrubs, and other changes in the surface. As a result, 24% of the annual radiative forcing was a result of fire-induced albedo changes during summer (May-September).

During the first year immediately following fire, the annual radiative forcing from surface albedo change was smaller than the 3-5 year mean. This was because charred surfaces and exposure of black carbon on the soil surface during the summer after the fire reduced albedo below that observed at nearby unburned conifer stands (*28*). After 3-5 years, the establishment of grasses, shrubs, and mosses and other changes to the surface increased summer albedo above pre-burn levels (Fig. 1). To estimate the radiative forcing during the first year, we assumed surface albedo within the Donnelly Flats perimeter in July, August, and September after the June 1999 fire was 0.07 (*28*). During winter and spring, and summer we used our observations (e.g., Fig. 1) to estimate surface albedo. We also assumed that the attenuation of outgoing shortwave radiation by clouds and atmospheric constituents was the same as for the 2002-2004 period: specifically that the difference in outgoing shortwave radiation at the tropopause was 60% of the difference at the surface. This yielded a year 1 albedo-driven radiative forcing of -5.4 ± 2.2 W m^{-2}, with the error estimate including ± 1.2 W m^{-2} from uncertainty in the albedo measurements and ± 1.0 W m^{-2} from a subjective assessment of the uncertainty associated with using the CRM.

1.6 Post-fire trajectory of surface albedo radiative forcing derived from MODIS

We extracted MODIS shortwave albedo (black sky and white sky) in interior Alaska to assess how long fire-induced changes in surface albedo persist during succession. The MODIS albedo product has a 16 day time step and a 1 km spatial resolution (*29*). Validation studies show that MODIS satellite-derived albedo agrees well with available field measurements, especially under snow-free conditions (*30*). Surface albedo was retrieved from the MODIS daily cloud-free atmospherically corrected directional surface reflectance using a semi-empirical bidirectional reflectance distribution model (BRDF) (*31*). The associated quality assurance fields are also stored in the operational product to provide information on the algorithm and product quality.

The black sky and white sky albedo products represent the fraction of radiation reflected by the surface under two extreme conditions. Black sky albedo represents the fraction of reflection when incoming light is in a direct beam whereas white sky albedo represents the fraction of reflection when the light source is isotropic diffuse. The albedo under realistic incoming solar radiation can be approximated as the combination of these two as a function of the fraction of direct and diffuse radiation (*31, 32*). Here we extracted the MODIS BRDF parameters to calculate the black sky albedo every 3 hours with the MODIS RossThickLiSparse BRDF model, since the MODIS black sky albedo was operationally produced only at local solar noon. The actual albedo was then derived as a sum of black sky albedo and white sky albedo weighted by the fraction of direct and diffuse surface incoming shortwave radiation. We used the monthly 3-hourly direct and

diffuse shortwave radiation data derived with the shortwave algorithm of the NASA World Climate Research Programme /Global Energy and Water-Cycle Experiment (WCRP/GEWEX) Surface Radiation Budget (SRB) Project (*33*). The radiation data were obtained from the Langley Atmospheric Sciences Data Center (http://eosweb.larc.nasa.gov/PRODOCS/srb/table_srb.html).

We identified burn perimeters using the Alaska fire history geographic information system (GIS) database from the Alaska Fire Service (AKFIREHIST; http://agdc.usgs.gov/data/blm/fire/index.html). In our analysis, we used fire perimeters from the beginning of the observed record (1950) through 2003 and MODIS data from 2000-2004. We excluded areas within 20 km of roads and towns to avoid post-fire trajectories that were substantially modified by human activity such as agriculture or development. We also imposed a 2 km buffer on the edge of burn perimeters to avoid possible geolocation errors. Another 1 pixel buffer on the outside of fire perimeters was excluded from our control areas (described below). Pixels identified as lakes, rivers, or water from a MODIS-derived vegetation cover map were also excluded (*34*). We also excluded pixels for a given time interval that did not pass MODIS quality assurance tests.

To derive the post-fire albedo trajectory, we calculated the mean albedo of all 1 km pixels that burned in a specific year for each 16-day MODIS interval. We did not include years for which there were fewer than 10 fire pixels or less than 2 fires. We constructed a pre-fire control albedo (shown by a dash dotted line in Fig. 2 in the main text) from the mean of all pixels within interior Alaska that did not burn during 1950-2003 and that were identified as evergreen conifer vegetation (*34*).

We assumed that the post-fire trajectory of albedo-driven radiative forcing followed MODIS albedo (Fig. 2A, dashed line, right axis). Albedo-driven radiative forcing increased from -5.0 W m^{-2} in year 1 to -8.5 W m^{-2} in year 10. During a deciduous phase (years 10-30), radiative forcing remained constant at -8.5 W m^{-2} reflecting sustained levels of elevated albedo during both spring and summer (Fig. 2). After year 30, radiative forcing decreased linearly, and was assumed to equal zero at year 55 and for all subsequent years. Averaged over years 0-80, albedo-driven radiative forcing was -4.2 ± 2.0 W m^{-2}. For this longer interval, our error estimate includes the components described above for years 3-5 (uncertainty from interannual variability in snow cover and use of the CRM) as well as an additional 20% reflecting uncertainty associated with estimating the post-fire trajectory of albedo from MODIS.

1.7 Ozone radiative forcing

The radiative forcing of ozone produced from the 2004 fire complex in Alaska and Yukon was estimated using the National Center for Atmospheric Research (NCAR) Community Atmosphere Model (CAM 3) by comparing model simulations that included fire emissions to a reference simulation where these emissions were turned off. The total fire emissions for the 2004 fire season were optimized weekly to match Measurements Of Pollution In The Troposphere (MOPITT) satellite observations of column CO over northern North America (*35*). This yielded total emissions of 30 Tg CO and a global annual mean O_3 atmospheric perturbation for the first year of 0.9 Tg O_3 – although most of the ozone was concentrated in the northern part of the northern hemisphere during summer. The burned area of the complex was approximately 4.45 x

10^{10} m^2. When normalized to the carbon emissions estimates we obtained for the Donnelly Flats fire (1560 ± 610 g C m^{-2}), this led to an adjusted radiative forcing from ozone of 6 W per m^2 of burned area, with an error estimate of 4 W m^{-2} that included uncertainties in the emissions, the optimization (*35*), emission ratios (*19*), and the radiative transfer calculations. Our approach for obtaining the adjusted radiative forcing from the instantaneous forcing at the top of atmosphere (that was readily available from CAM 3) is provided in more detail in section 1.11 and table S1.

1.8 Instantaneous aerosol and snowpack radiative forcing

We simulated black carbon (BC) and organic carbon (OC) aerosol direct radiative forcing from the Donnelly Flats fire using CAM 3 (*36*). We used emissions described in section 1.1, applying BC and OC emission factors from M. Andreae ((*19*), pers. comm.), injected uniformly over the 8-day fire period. Aerosol optical properties were prescribed (*37*). Aerosols were injected into the lowest atmospheric layer, and hydrophobic BC and OC was transformed to hydrophilic components with an e-folding time of 1.2 days. We estimate global shortwave (0.3-5.0 μm) instantaneous top of atmosphere (TOA) radiative forcing from atmospheric BC and OC and surface forcing from BC in snow and ice with an ensemble of two 10 year simulations (fig. S9). In each simulation, fire emissions were injected into the model during June 11-18. Given that almost all of the instantaneous radiative forcing from both atmospheric aerosols and their deposition on snow and sea ice had dissipated after 6 months, this allowed for 10 independent model realizations within each run.

Snow radiative processes and aging were simulated with the SNow, ICe, and Aerosol Radiative model (SNICAR) (*38*), based on Warren and Wiscombe (*39*) and Toon et al. (*40*), and coupled to CAM 3. Factors which control snow and ice forcing include aerosol transport mechanisms, snow grain size, meltwater scavenging efficiency, BC optical properties, surface incident flux, and snow cover fraction. Very small quantities of BC can reduce snow reflectance (*39, 41*). For the changes in snow albedo caused by the deposition of BC, we assumed that instantaneous forcing at the tropopause was equal to 0.92 of the surface forcing based on a series of offline experiments with the Shortwave Narrowband (SWNB) atmospheric model (*42*) with varying albedo perturbation, cloud thickness, and aerosol absorption optical depth. We assumed that stratospheric readjustment was minimal, so that instantaneous tropopause forcing was approximately equal to the definition of radiative forcing given by the IPCC (*2, 3*).

About 89% of the direct radiative forcing from the atmospheric aerosols occurred immediately after the fire during the latter part of June. Another 11% occurred during July, with negligible contributions in subsequent months. The annual radiative forcing from atmospheric aerosols was 17 ± 30 W m^{-2}. Our error estimate includes a large component caused by interannual variability in climate within CAM 3. Interannual variability in wind direction and strength at the point source, near-source snow and cloud conditions, and precipitation patterns influenced aerosol lifetimes and the strength of their forcing. At the surface, the perturbation to net shortwave radiation from both aerosol absorption and scattering was substantially larger and led to a net cooling of -90 ± 35 W m^{-2}.

The combined radiative forcing from BC deposition on snow and sea ice albedo was 8 ± 5 W m^{-2}. Our error estimate includes interannual variability in model transport of BC to areas covered by snow and sea ice as well as uncertainty associated with modeling the radiative effects of BC on snow and ice albedo.

1.9 Stand age modeling

We constructed a grid with 1 x 10^5 cells, each with a unique age and each cell representing a single boreal forest stand. The probability of a cell burning (and having its age reset to zero) was set in the model to be a function of cell age. The probability of fire was suppressed in cells during the first 30 years and then increased to a constant final probability that remained constant for cells older than 55 years. The initial probability of fire was set equal to 1/5 of the final probability in our model simulations. This parameterization was based on an analysis of Alaskan burn perimeters (from the last 55 years (*43*)) that showed fires were more likely to occur in older rather than younger stands as compared to a probability distribution obtained from assuming fire did not depend on stand age. This parameterization generates a stand age distribution similar to that obtained from a Weibull function, which has been used in the past to model boreal forest stands (*44*). In terms of the underlying mechanism, suppression of fire in younger stands may occur from a delayed and slow build up of flammable fuels in the first few decades after fire and also from a higher water content of deciduous vegetation that often establishes immediately after fire (*44*).

In each model run, we stepped the model forward at 1 year increments out to 600 years. At each time step, the probability of fire in each cell was evaluated using the fire probability function described above (that was a function of the cell age) and a random number generator. At the end of each model run, we convolved the resulting stand age distribution with the post-fire trajectory of radiative forcing (for each agent) to compute a stand age-weighted radiative forcing mean.

For the greenhouse gas trajectories, we assumed a constant background CO_2 concentration (380 ppm) and we used ocean impulse functions from the pre-industrial period from Joos and Siegenthaler (*24*). These two adjustments were made (as compared to the approach taken in section 1.4) so that we could examine radiative forcing from a contemporary change in the fire regime in Fig. 3C. In a series of model runs, we varied the final probability of fire between 0.0055 and 0.03 at increments of 0.001. The resulting radiative forcing values are shown in Fig. 3C, assuming the stand age distribution starts at steady state with a mean fire return time of 80 years. We arbitrarily chose a mean of 80 years here for consistency with the stand age of our control - across the boreal biome fire return times vary widely (*44*). We could have added a different set of offsets so that the sum of different forcing agents was zero with a mean fire return time at steady state at 100 or 120 years. These adjustments would not change the slope of the lines in Fig. 3C or our conclusions. We also generated a series of stand age distributions assuming that the probability of fire did not depend on stand age (exponential distributions). These latter stand age distributions did not substantially change the slopes of the lines shown in Fig. 3C.

1.10 Other forcing agents

For the sake of brevity we did not consider several additional smaller forcing agents in the main text. Specifically, a small amount of heat is released directly from the oxidation of organic matter during combustion. Assuming fuels at Donnelly Flats had a heat of formation of 20.9 KJ/g and that organic matter was comprised of 50% carbon, the fire emissions pulse would have been accompanied by 65 MJ of heat released into the atmosphere. Averaged over year 1, this corresponds to 2 W m^{-2}, but not all of this would correspond to radiative forcing; some infrared radiation would be lost to space and would not contribute to atmospheric heating. Further, over 80 years, the net effect of this oxidation flux would be nearly zero because this is the time for biomass (and chemical energy) accumulation within the ecosystem to equal that lost during the initial fire event. We also did not consider aerosol indirect effects, including a reduction in cloud droplet size and extended cloud lifetimes. Although uncertain, the sum of all aerosol indirect effects are thought to contribute to a negative radiative forcing (*1, 3, 45*).

1.11 Approach for estimating adjusted and effective forcings

In the main text we report radiative forcing after the stratosphere has adjusted radiatively, following the IPCC TAR convention (*1*). This forcing, hereafter referred to as F_a, has been shown to be more closely linked with the equilibrium temperature response in climate models than other types of radiative forcing (*2*), but was not immediately available for a number of the agents that we examined here in the context of the Donnelly Flats fire. As a result, in some cases we needed to convert the instantaneous forcing at the top of atmosphere ($F_{i,toa}$) or at the tropopause ($F_{i,tropo}$) to F_a. For a number of agents, including post-fire albedo changes, BC deposition on snow and sea ice, and fire-emitted aerosols, the differences between $F_{i,toa}$, $F_{i,tropo}$, and F_a were relatively small. For ozone the differences were larger. We relied on our own radiative transfer modeling to convert between $F_{i,toa}$ and $F_{i,tropo}$, and then on published estimates from climate models (*2, 3*) to convert in a second step between $F_{i,tropo}$ and F_a. Hansen et al. (2) and Hansen et al. (3) provide background information on the relationship between these different types of radiative forcing, hereafter we refer to these two studies as H97 and H05.

We also report here in section 2 (SOM text) and in the footnote to Table 1 in the main text, the effective forcing from the different agents, taking into account that the global temperature response per unit of forcing varies depending on the agent (*3*). Note that the efficacy values we report in Table S1 are relative to F_a and are derived from H05.

Myhre et al. (23) provide equations for directly computing F_a from atmospheric concentrations of CO_2 and CH_4 and so we did not need to convert between instantaneous and adjusted forcings. The efficacy of forcing agents is defined relative to the forcing from CO_2, so by definition CO_2 has an efficacy of 1.0 (*3*). The efficacy for methane is approximately 1.45 because methane indirectly contributes to stratospheric water vapor and tropospheric ozone (*3*).

For ozone, we estimated $F_{i,toa}$ from simulations with the NCAR Community Atmosphere Model (CAM 3) as described in section 1.7 above. We then used the vertical profile of the ozone anomaly from CAM 3 with the CRM model (described in section 1.5) to estimate $F_{i,tropo}$. In a second step, we assumed that the ratio of $F_{i,tropo}$ to F_a from ozone emitted from the Donnelly Flats fire was the same as that derived from

tropospheric ozone simulations with the GISS model (*3*). The efficacy for forcing associated with increases in tropospheric ozone is approximately 0.82 (*3*).

To estimate F_a from BC deposition on remote snow and sea ice, we first obtained $F_{i,tropo}$ based on the approach is described in section 1.8. In a second step, we assumed that $F_{i,tropo}$ was equal to F_a for snow and sea ice forcing from Donnelly Flats fire based on climate model simulations of changes in surface albedo (as shown in Table 11 of H97). The efficacy for black carbon deposition is thought to be relatively large (1.7) because of snow and ice feedbacks (*3*).

To estimate F_a from aerosols emitted by the Donnelly Flats fire, we first obtained $F_{i,toa}$ from the CAM 3 (the approach is described in section 1.8). Based on simulations from the SWNB model, we estimated that $F_{i,tropo}$ was slightly larger than $F_{i,toa}$ ($F_{i,tropo} = F_{i,toa}$ *1.01). In a second step, we assumed that $F_{i,tropo}$ was approximately equal to F_a for aerosol forcing from the Donnelly Flats fire based on global climate model simulations with tropospheric aerosols (Table 10 from H97 and Table 2 from H05). For aerosols, we used an efficacy of -0.2 based on Table 5 of H05. This value was negative because forcing from OC aerosols has a substantially higher efficacy (0.91) than forcing from BC aerosols (0.58). More specifically, because the net forcing from biomass burning aerosols reflects a balance between a large positive component associated with absorptive BC and a large negative component associated with reflective OC, a smaller efficacy for the positive term can flip the sign of the net effective forcing.

To estimate F_a from the changes in surface albedo within the Donnelly Flats burn perimeter, we first obtained $F_{i,tropo}$ from CRM, driving the model with observations of surface albedo and incoming shortwave radiation at our field sites (the approach is described in section 1.5). As with the snow and sea ice forcing approach described above, in a second step we assumed that the ratio $F_{i,tropo}$ was the same as F_a based on northern surface albedo simulations obtained from a global climate model (Table 11 from H97).

2. Supporting text

Feedbacks We used the concept of radiative forcing to compare the different ways by which fire influences climate. As noted in the main text an important next step is to quantify feedbacks. One important feedback that may contribute to cooling with increased fire activity is the replacement of conifer stands with broadleaf deciduous stands. High mid-summer evapotranspiration fluxes associated with broadleaf deciduous trees (*12, 28, 46*) may increase cloud cover and planetary albedo, and thus contribute to additional cooling.

In contrast, over centennial to millennial time scales, increased deposition of black carbon on sea ice and the Greenland ice sheet may accelerate surface melting and mass loss. Reductions in aerial extent of the Greenland ice sheet would substantially decrease northern albedo and thus would represent a strong positive feedback to warming (apart from impacts on sea level and ocean circulation).

Effective forcings Following the approach by H05, we also estimated effective forcings (F_e). These forcings were obtained by multiplying the adjusted forcings in Table 1 of the main text (F_a) by the efficacy values reported in Table S1. In terms of F_e, the net effect of the Donnelly Flats fire was -2.4 ± 2.3 W m^{-2} over the 80-year fire cycle (Table S2), reflecting a slightly larger cooling impact of fire than what we obtained from the total adjusted forcing (-2.3 ± 2.2 W m^{-2} as reported in Table 1 of the main text).

3. Supporting figures

Fig S1. Photo of the Donnelly Flats fire that occurred during 11-18 June 1999. This photo was taken on 13 June 1999 from Fort Greely looking south towards the fire front and the Alaska Range. Photo credit: Kerensa Hardy, Ft. Greely Public Affairs, U.S. Army. Reproduced by permission of the Delta News Web.

Fig S2. Photo of the Donnelly Flats fire on Fort Greely. Photo credit: Tom Lucas. Reproduced by permission of the Delta News Web.

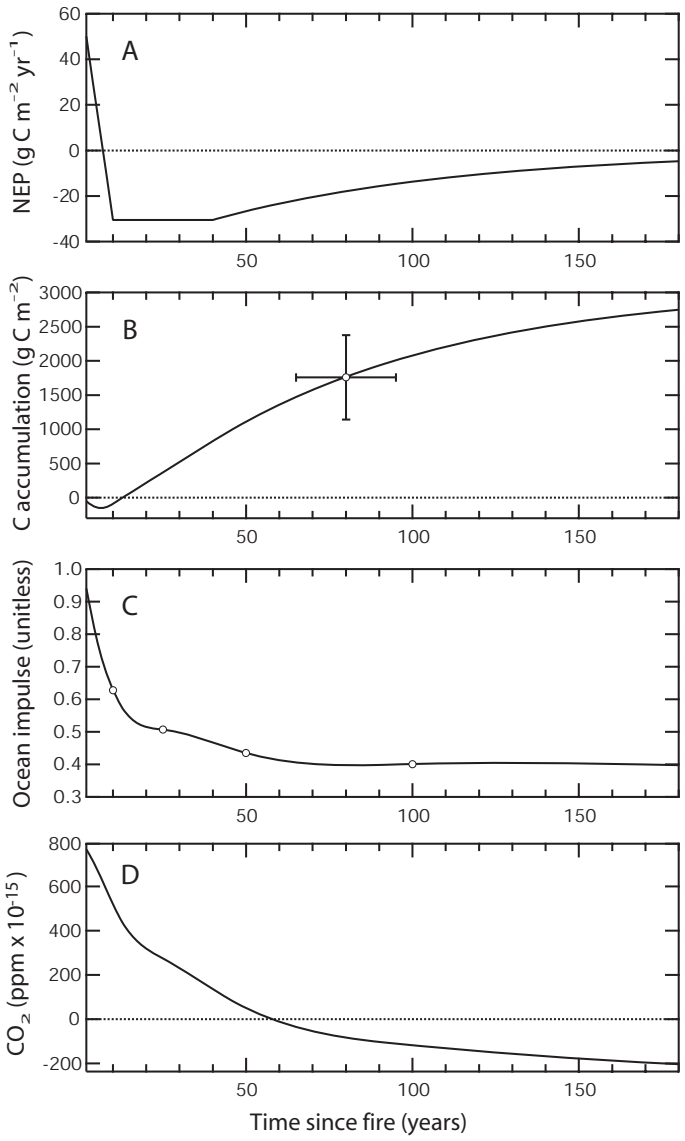

Fig. S3. A) Trajectory of net ecosystem production (NEP) constructed with the constraint that carbon accumulation over the first 80 years was equal to carbon loss during the first year of the Donnelly Flats fire and that uptake rates were highest during a deciduous phase from 10 to 40 years. B) Trajectory of total carbon accumulation (the integral of A). The point represents the measured total carbon loss during the Donnelly Flats fire and was obtained by a comparison of carbon inventories within the burn perimeter to carbon inventories from the approximately 80-year adjacent control stand. C) The fraction of atmospheric CO_2 pulse (injected at time 0 and with strength of 1 unit) that remains airborne as a function of time, as a result of ocean-atmosphere gas exchange. This impulse function was constructed assuming the injection occurred during contemporary times (during the 1990s) and that CO_2 concentrations continue to increase until they stabilize at 650 ppm at the end of the century (*24*). D) The global CO_2 anomaly from the Donnelly Flats fire (per m^2 of emissions). This anomaly reflects uptake of the fire CO_2 pulse by both the oceans and by regrowing vegetation within the fire scar.

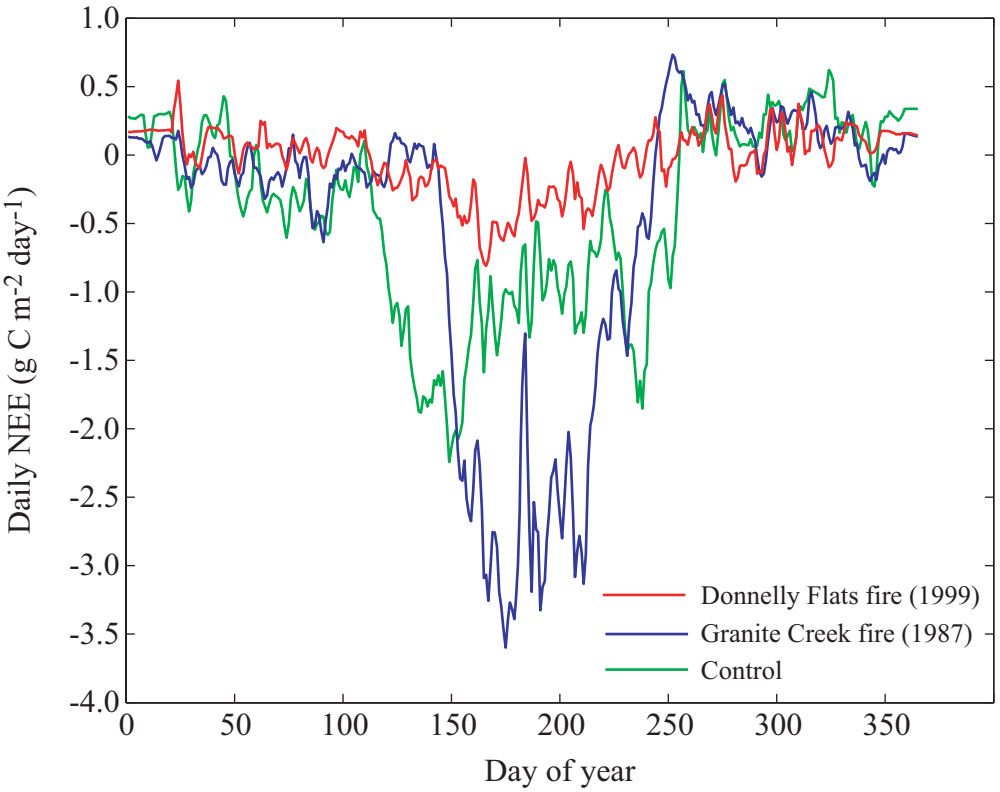

Fig. S4. Daily net ecosystem exchange measured by eddy covariance at the Donnelly Flats fire (1999), the Granite Creek fire (1987), and the control stand averaged over 2002-2004.

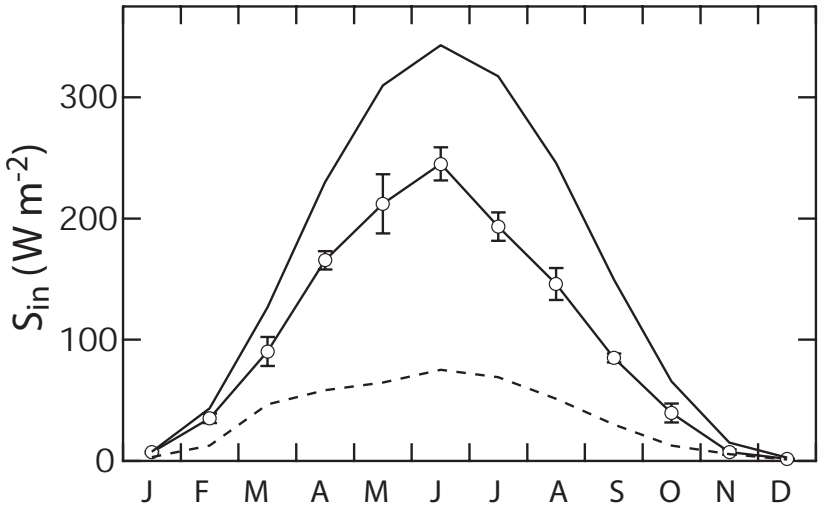

Fig. S5. Observations of incoming shortwave radiation (S_{in}) from our field sites near Delta Junction, Alaska (circles with standard deviation error bars) fall in between column radiation model (CRM) estimates for clear sky (solid line) and cloudy conditions (dashed line). The measurements of S_{in} represent the monthly mean of 3 years (2002-2004) from two radiometers (one at each of the burn and control sites). Standard deviation error bars primarily reflect interannual variability in cloudiness for a given month.

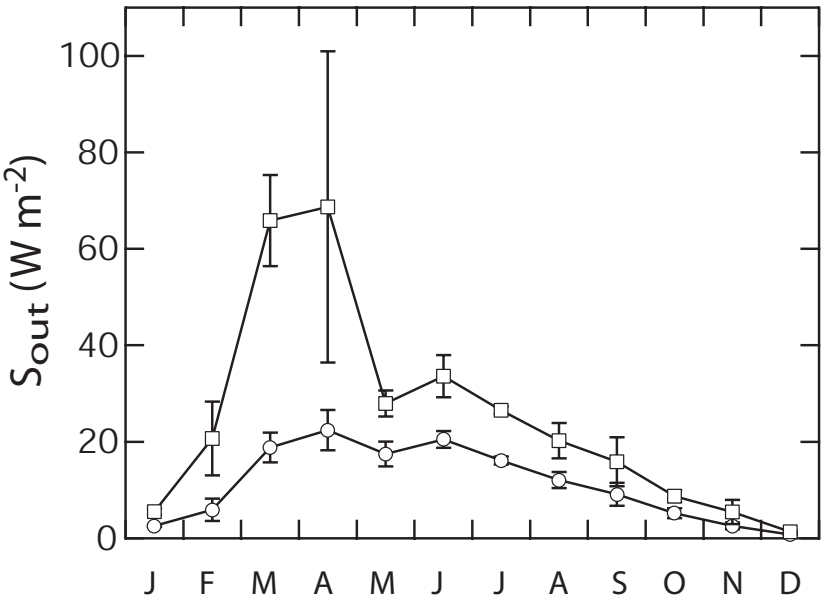

Fig. S6. Observations of outgoing shortwave radiation (S_{out}) from the control (circles) and burn (squares), measured using radiometers above the canopy and averaged over 2002-2004. The difference in S_{out} at the tropopause (after attenuation by clouds and other atmospheric constituents in the troposphere) is approximately equal to the radiative forcing from the fire-induced change in surface albedo. Interannual variability in S_{out} (shown with the standard deviation error bars) was greatest during April, primarily as a result of year-to-year differences in the timing of snowmelt.

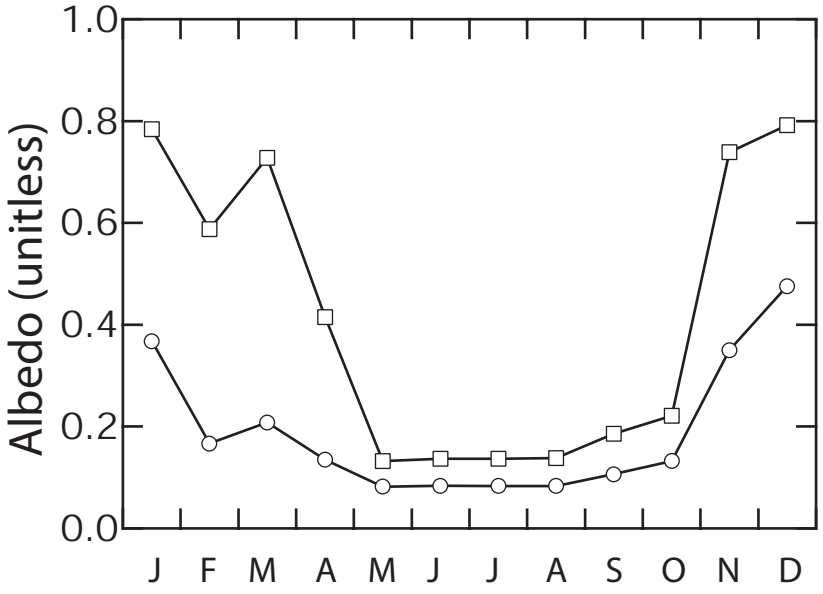

Fig. S7. Monthly mean surface albedo from the control stand (circles) and from within the Donnelly Flats burn perimeter (squares) during 2002-2004.

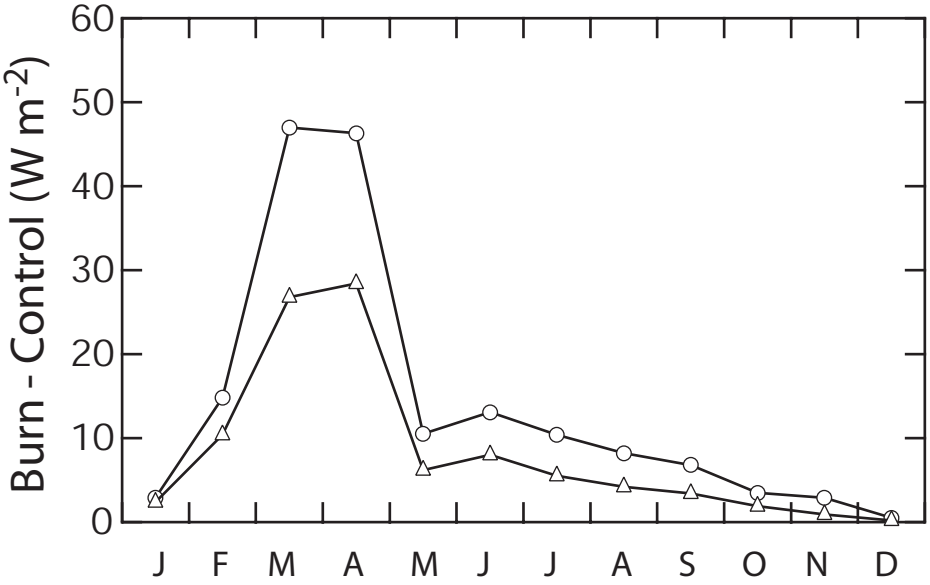

Fig. S8. Difference in outgoing shortwave radiation between the burn and control at the surface (circles) and at the tropopause (triangles). The tropopause shortwave radiation difference was estimated using the Column Radiation Model described in the Supporting Online Methods section 1.5.

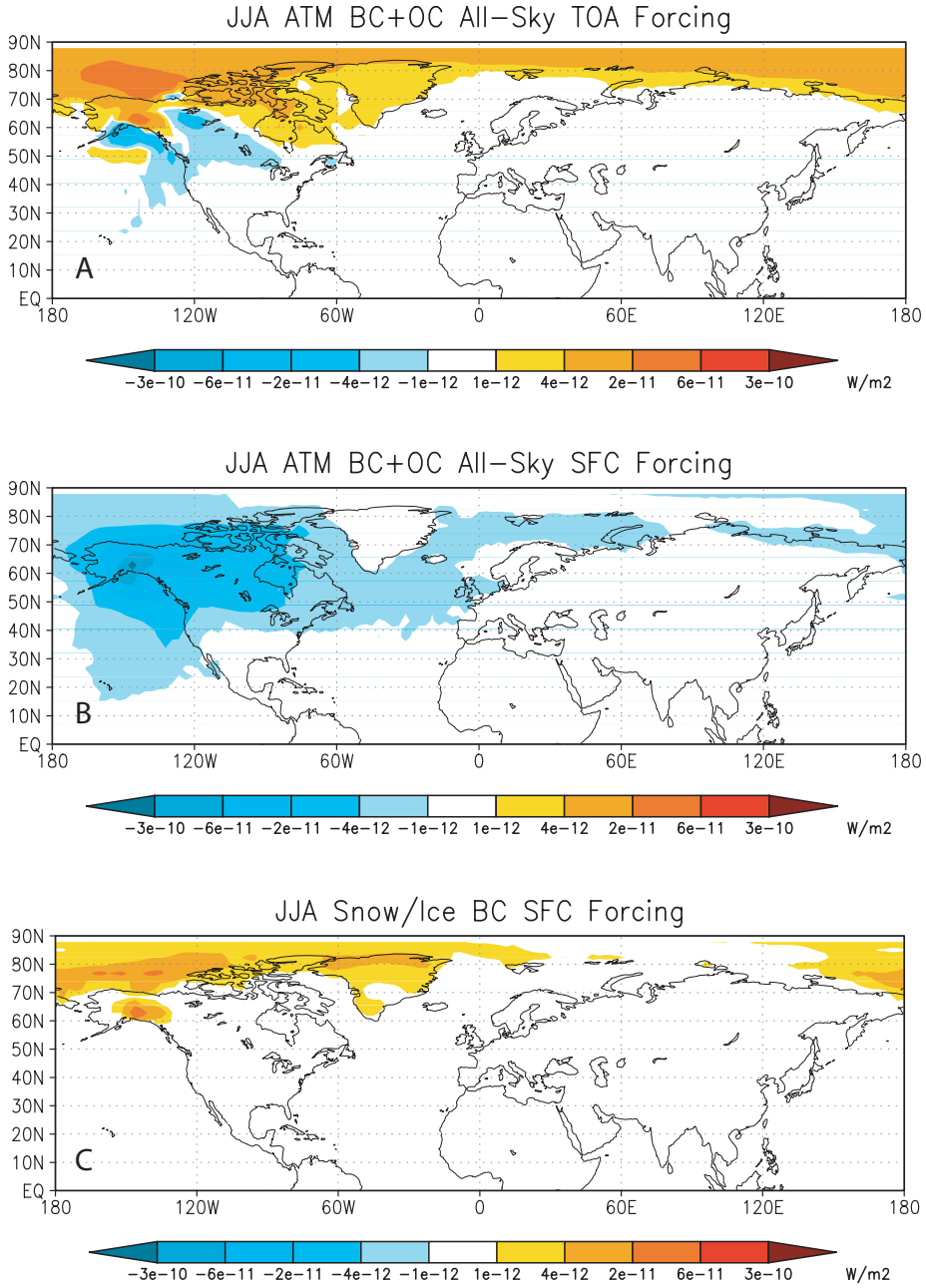

Fig. S9. A) Top of atmosphere instantaneous radiative forcing from aerosols emitted from the Donnelly Flats fire for all-sky conditions (including both clear sky and cloudy conditions) was concentrated primarily in boreal and arctic regions. B) At the surface, the perturbation to net shortwave radiation from both aerosol absorption and scattering was substantial and led to a net cooling of -90 ± 35 W per m^{-2} of burned area. C) Surface forcing from black carbon deposition primarily occurred on sea ice, the Greenland ice sheet, and snow in the Alaska Range. All of these estimates were derived from the NCAR CAM 3. Note that the color scale is logarithmic.

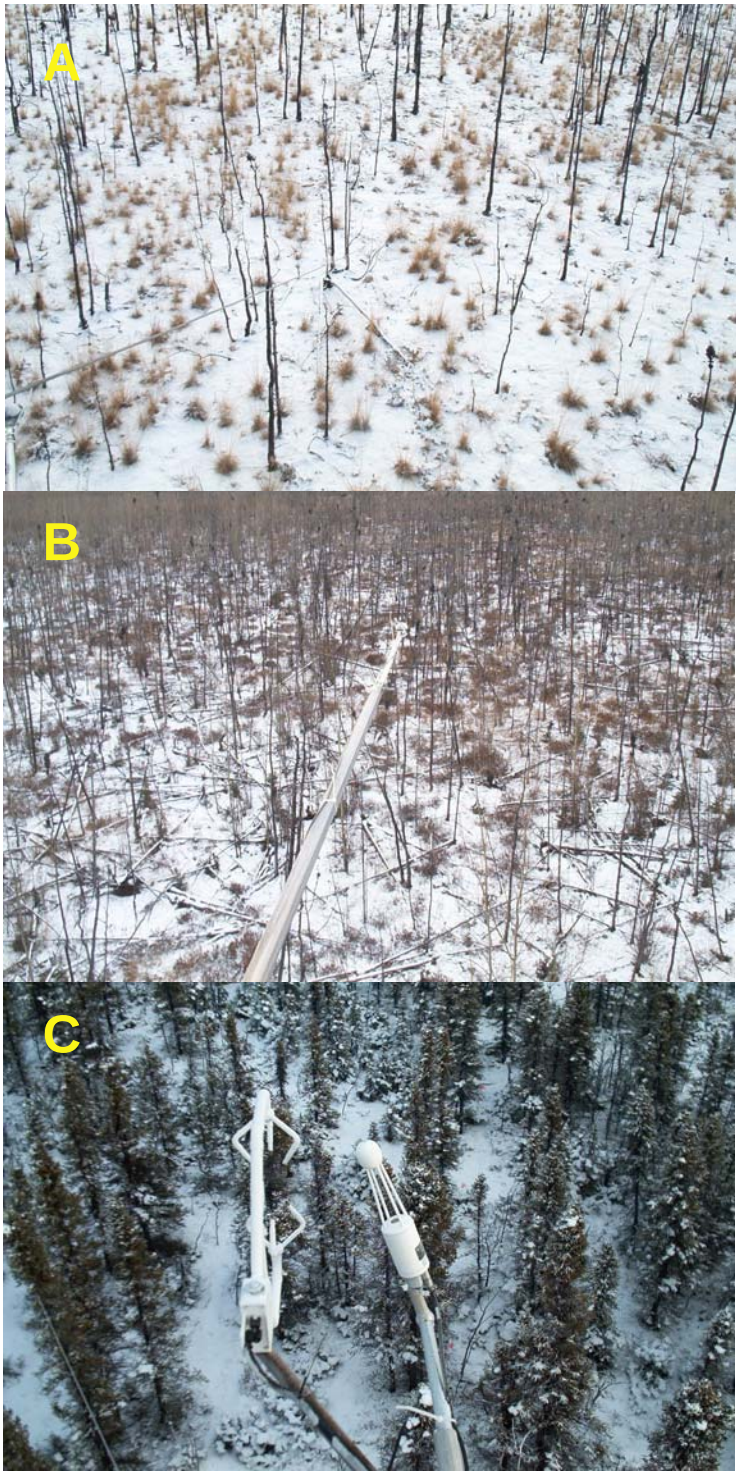

Fig. S10. Photographs of the Donnelly Flats stand that burned in 1999 (A), the Granite Creek stand that burned in 1987 (B), and the control stand that burned in approximately 1920. These photographs were taken from the eddy covariance towers at these sites on 30 November 2002.

4. Supporting tables

Table S1. The relationship between different forcing estimates and their efficacy

Agent	$F_{i,tropo}$[a] / $F_{i,toa}$	F_a / $F_{i,tropo}$	Efficacy[b]
Greenhouse gases			
CO_2	N/A	N/A	1.00
CH_4	N/A	N/A	1.45
Ozone	1.30	0.83	0.82
Black carbon deposition on snow	N/A	1.00	1.7
Black carbon deposition on sea ice	N/A	1.00	1.7
Aerosols (net)	1.01	1.00	-0.20
black carbon	1.01	1.04	0.58
organic carbon	1.01	0.98	0.91
Changes in post-fire surface albedo	N/A	1.00	1.02

a. $F_{i,tropo}$ is the instantaneous radiative forcing at the tropopause, $F_{i,toa}$ is the instantaneous radiative forcing at the top of atmosphere, and F_a is the adjusted forcing (the IPCC TAR convention).
b. We obtained these efficacy estimates from H05.

Table S2. Effective radiative forcing (F_e) associated with the Donnelly Flats fire

Forcing agent:	Radiative forcing[a], W (m^2 burned)$^{-1}$	
	Year 1	Years 0-80 (mean)
Long-lived greenhouse gases (CO_2 and CH_4)	9 ± 4	1.7 ± 0.9
Ozone	5 ± 4	0.1 ± 0.0
Black carbon deposition on snow	5 ± 5	0.1 ± 0.1
Black carbon deposition on sea ice	9 ± 7	0.1 ± 0.1
Aerosols (direct radiative forcing)[b]	-3 ± 40	0.0 ± 0.5
Impact at the surface: -90 W ± 35 m^{-2}		
Changes in post-fire surface albedo	-5 ± 2	-4.3 ± 2.1
Total	18 ± 41	-2.4 ± 2.3

a. Radiative forcing here refers to effective forcing (F_e) following the approach described by Hansen et al. (2005) and as described in section 1.11. Efficacy values from Table S1 were applied to the adjusted forcing estimates provided in Table 1 of the main text.
b. The aerosol forcing changed sign from 17 W m^{-2} to -3 W m^{-2} and the uncertainties increased as a result of applying the efficacy values from Table S1.

5. Supporting references and notes

1. V. Ramaswamy *et al.*, in *Climate Change 2001: The Scientific Basis. Contributions of Working Group 1 to the Third Assessment Report of the Intergovernmental Panel on Climate Change* J. T. Houghton *et al.*, Eds. (Cambridge University Press, Cambridge, United Kingdom and New York, NY, USA, 2001) pp. 350-416.
2. J. Hansen, M. Sato, R. Ruedy, *Journal of Geophysical Research-Atmospheres* **102**, 6831 (1997).
3. J. Hansen *et al.*, *Journal of Geophysical Research-Atmospheres* **110**, 10.1029/2005JD005776 (2005).
4. T. R. Crow, *Ecology* **59**, 265 (1978).
5. J. C. Neff, J. W. Harden, G. Gleixner, *Canadian Journal of Forest Research-Revue Canadienne De Recherche Forestiere* **35**, 2178 (2005).
6. D. U. Hooper, Z. I. Cardon, C. F. S. III, M. Durant, *Oecologia* **132**, 1 (2002).
7. E. K. Webb, G. I. Pearman, R. Leuning, *Quarterly Journal of the Royal Meteorological Society* **106**, 85 (1980).
8. D. D. Baldocchi, B. B. Hicks, T. P. Meyers, *Ecology* **69**, 1331 (1988).
9. T. W. Horst, *Boundary-Layer Meteorology* **82**, 219 (1997).
10. W. Eugster, W. Senn, *Boundary-Layer Meteorology* **74**, 321 (1995).
11. S. D. Chambers, J. M. Hacker, A. G. Williams, "The RAMF Users' Manual (Version 8.1)." *Tech. Report No. Technical Report No. 14.* (The Flinders University of South Australia, 1996).
12. H. P. Liu, J. T. Randerson, J. Lindfors, F. S. Chapin, *Journal of Geophysical Research-Atmospheres* **110**, 10.1029/2004JD005158 (2005).
13. L. R. Welp, J. T. Randerson, H. P. Liu, *Journal of Geophysical Research-Biogeosciences* **111**, 10.1029/2005JG000126 (2006).
14. M. L. Goulden *et al.*, *Science* **279**, 214 (1998).
15. S. E. Trumbore, J. W. Harden, *Journal of Geophysical Research-Atmospheres* **102**, 28817 (1997).
16. B. Bond-Lamberty, C. K. Wang, S. T. Gower, *Global Change Biology* **10**, 473 (2004).
17. K. P. O'Neill, E. S. Kasischke, D. D. Richter, *Journal of Geophysical Research-Atmospheres* **108**, 10.1029/2001JD000443 (2003).
18. F. S. I. Chapin *et al.*, *Ecosystems* **In Press.** (2006).
19. M. O. Andreae, P. Merlet, *Global Biogeochemical Cycles* **15**, 955 (2001).
20. T. M. Butler, P. J. Rayner, I. Simmonds, M. G. Lawrence, *Journal of Geophysical Research-Atmospheres* **110**, 10.1029/2005JD006071. (2005).
21. J. S. Daniel, S. Solomon, *Journal of Geophysical Research-Atmospheres* **103**, 13249 (1998).
22. M. J. Prather, *Geophysical Research Letters* **23**, 2597 (1996).
23. G. Myhre, E. J. Highwood, K. P. Shine, F. Stordal, *Geophysical Research Letters* **25**, 2715 (1998).

24. I. G. Enting, T. M. L. Wigley, M. Heimann, "Future Emissions and Concentrations of Carbon Dioxide: Key Ocean/Atmosphere/Land Analyses" (Technical paper no. 31, CSIRO Division of Atmospheric Research, 2001).
25. B. P. Briegleb, *Journal of Geophysical Research-Atmospheres-Atmospheres* **97**, 7603 (1992).
26. J. T. Kiehl *et al.*, "Description of NCAR Community Climate Model (CCM3)" *Tech. Report No. TN-420* (National Center for Atmospheric Research, 1996).
27. S. M. Uppala *et al.*, *Quarterly Journal of the Royal Meteorological Society* **131**, 2961 (2005).
28. S. D. Chambers, F. S. Chapin, *Journal of Geophysical Research-Atmospheres* **108**, 10.1029/2001JD000530 (2002).
29. C. B. Schaaf *et al.*, *Remote Sensing of Environment* **83**, 135 (2002).
30. Y. F. Jin *et al.*, *Journal of Geophysical Research-Atmospheres* **108**, 10.1029/2002JD002803 (2003).
31. W. Lucht, C. B. Schaaf, A. H. Strahler, *Ieee Transactions on Geoscience and Remote Sensing* **38**, 977 (2000).
32. P. Lewis, M. Barnsley, paper presented at the International Symposium on Physical Measurements and Signatures in Remote Sensing, Int. Sco. for Photogramm. and Remote Sens., Vald'Isere, France. 1994.
33. R. T. Pinker, I. Laszlo, *Journal of Climate* **5**, 56 (1992).
34. M. A. Friedl *et al.*, *Remote Sensing of Environment* **83**, 287 (2002).
35. G. Pfister *et al.*, *Geophysical Research Letters* **32**, 10.1029/2005GL022995 (2005).
36. P. J. Rasch, W. D. Collins, B. E. Eaton, *Journal of Geophysical Research-Atmospheres* **106**, 7337 (2001).
37. M. Hess, P. Koepke, I. Schult, *Bulletin of the American Meteorological Society* **79**, 831 (1998).
38. M. G. Flanner, C. S. Zender, *Journal of Geophysical Research* **111**, D12208 (2006).
39. S. G. Warren, W. J. Wiscombe, *Journal of the Atmospheric Sciences* **37**, 2734 (1980).
40. O. B. Toon, C. P. McKay, T. P. Ackerman, K. Santhanam, *Journal of Geophysical Research-Atmospheres* **94**, 16287 (1989).
41. A. D. Clarke, K. J. Noone, *Atmospheric Environment* **19**, 2045 (1985).
42. C. S. Zender *et al.*, *Journal of Geophysical Research-Atmospheres* **102**, 29901 (1997).
43. The Alaska Fire Service maintains a database of annual fire statistics and geographic information system (GIS) burn perimeters (http://agdc.usgs.gov/data/blm/fire/).
44. E. A. Johnson, *Fire and Vegetation Dynamics: Studies from the North American Boreal Forest*. H. J. B. Birks, Ed., Cambridge Studies in Ecology (Cambridge University Press, 1992), pp. 127.
45. V. Ramanathan, P. J. Crutzen, J. T. Kiehl, D. Rosenfeld, *Science* **294**, 2119 (2001).
46. D. Baldocchi, F. M. Kelliher, T. A. Black, P. Jarvis, *Global Change Biology* **6**, 69 (2000).